I&EC research
Industrial & Engineering Chemistry Research
pubs.acs.org/IECR
Article

In Situ Hydrothermal Conversion of Silica Gel Precursors to Binderless Zeolite X Pellets for Enhanced Olefin Adsorption

Hao Jiang, Dan Wang, Jialun Tan, Yuxiang Chen, Yang An, Yonghao Chen, Yuan Wu, Hui Sun,* Benxian Shen, Di Wu,* Jichang Liu, Hao Ling, Jigang Zhao, and Yujun Tong

Cite This: *Ind. Eng. Chem. Res.* 2020, 59, 9997−10009

ABSTRACT: Binderless zeolite X pellets were "one-pot"-synthesized *via* *in situ* hydrothermal conversion of silica gel precursors in sodium aluminate solution. The conversion and crystallization kinetics were investigated as a function of synthesis time with a spectrum of techniques. It is found that four-membered rings (4R) and six-membered rings (6R) are formed by linking diffused Al species with dissolved Si species during the aging period, whereas the zeolite X frameworks are constructed *via* reorganization of *β* cages with double six-membered rings (D6R) in a crystallization process. Furthermore, the grand canonical Monte Carlo simulation was conducted to elucidate 1-hexene adsorption on zeolite X with ion species and exchange degree variation. Specifically, the adsorption capacity and guest−host interaction energy were evaluated. Incorporation of Mg^{2+} and Ca^{2+} enables a higher adsorption capacity, whereas introduction of Co^{2+}, Ni^{2+}, Cu^{2+}, and Zn^{2+} boosts adsorption capacity and enhances interaction energy.

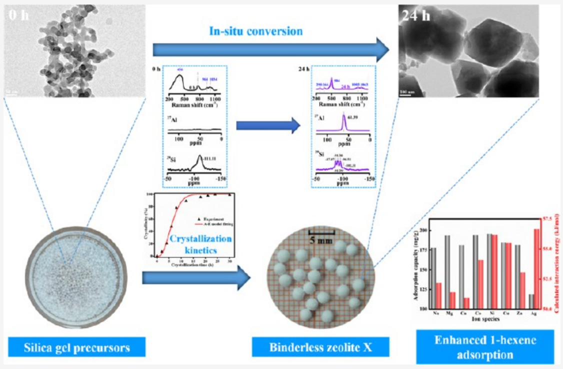

1. INTRODUCTION

Effective separation of olefin/paraffin is critical for the modern chemical industry,[1−4] in which olefins are primarily obtained from the hydrocarbon steam cracking mixtures to serve as feedstock.[5,6] Removal of impurities from olefins must be maximized to ensure the high quality of subsequently derived products.[7,8] Typical methods for olefin/paraffin separation include cryogenic distillation,[3,9] liquid−liquid extraction,[10] adsorptive separation,[11−13] and membrane separation.[14−16] Among all these approaches, adsorptive separation is considered to be a promising alternative compared to the current main technologies owing to its high selectivity and flexibility, mild operating condition, and low capital cost.[3,13,17] Indeed, successful adsorptive separation largely relies on the performance of adsorbents employed. During the past several decades, a variety of porous materials, including aluminosilicate zeolites,[12,18,19] carbon molecular sieves,[20,21] and metal−organic frameworks (MOFs),[22,23] have been extensively explored, tested, and applied for adsorptive separation of olefin/paraffin mixtures. Synthetic zeolites remain the most popularly utilized adsorbents in various industrial processes because of their high energetic and structural stability, and low cost.[24,25]

Ion-exchange has been primarily focused on tuning the pore structure and adsorption affinity to enhance adsorption capacity and selectivity.[26,27] According to earlier reports, a variety of ion-exchanged zeolite sorbents have been employed for selective adsorption of olefins over paraffins. Sakai *et al.*[28] reported that compared with the parent zeolite NaX membrane, the selectivity of an Ag-exchanged zeolite X membrane for olefins increased from 3.63 (NaX) to 55.4 (Ag−NaX) for a propylene/propane (50:50) mixture. In addition, Anson *et al.*[29] studied the effect of cation type on the performance of ion-exchanged ETS-10 in ethane/ethylene separation. They concluded that the adsorption selectivity of ethylene over ethane decreased following the order of Na > K > Li > Cu ≈ Ba > Ba/H > La/H. This trend appears to be completely opposite to the pressure swing adsorption results. Moreover, it was reported that Cu-exchanged natural Chilean zeolite, which mainly consists of clinoptilolite and mordenite, showed increased number of adsorption sites and enhanced interaction energy in ethylene adsorption, which led to significantly increased adsorption capacity.[30]

For practical applications, conventionally synthesized zeolite powder has to be fabricated as macroscale particles/pellets with additional binder to ensure relative low pressure drop across the sorbent bed.[31,32] Nevertheless, the binder introduced is an adsorption inert component, which results

Received: March 1, 2020
Revised: April 30, 2020
Accepted: May 5, 2020
Published: May 5, 2020

https://dx.doi.org/10.1021/acs.iecr.0c01049
Ind. Eng. Chem. Res. 2020, 59, 9997−10009

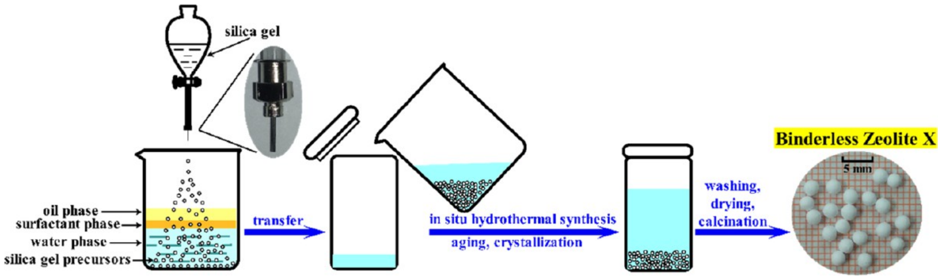

Figure 1. Schematics of *in situ* hydrothermal synthesis of binderless zeolite X pellets.

in reduced adsorption capacity.[31,33] Moreover, the binder component may lead to undesired side reactions and/or diffusion inhibition.[33,34] To minimize the negative impacts of the binder on the performance of industrial adsorbents, recently, we developed a one-pot route to synthesize binderless zeolite A pellets by using *in situ* hydrothermal transformation of silica gel precursors.[35]

In the current work, we report the synthesis of spherical binderless zeolite X pellets *via in situ* hydrothermal conversion of silica gel precursors. The synthesized binderless zeolite X exhibits significantly enhanced adsorption performance compared with commercially available binder-containing zeolite X products. Employing multiple analysis methodologies, we further characterized the resulting solid samples as the synthesis length varies and deduced the *in situ* conversion mechanism from precursors to zeolite X. Further, the impacts of ion type and exchange degree on olefin adsorption were evaluated experimentally by 1-hexene adsorption and computationally with the grand canonical Monte Carlo (GCMC) simulation, in which we successfully correlate adsorption capacity and guest−host interaction energy with type of cation and degree of exchange for 1-hexene adsorption on ion-exchanged zeolite X.

2. MATERIALS AND METHODS

2.1. Materials. Sodium metaaluminate (>98.5% purity) and cetyltrimethyl ammonium bromide (CTAB, >99.0% purity) were purchased from Aladdin Industrial Co., Ltd. (Shanghai, China). Sodium hydroxide (>96.0% purity) and ammonium chloride (>99.5% purity) were provided by Sinopharm Chemical Reagent Co., Ltd. (Shanghai, China). Silica sol (solid content of 40 wt %) with an average particle size of 20 nm was obtained from Qingdao Fuso Refining & Processing Co., Ltd. (Qingdao, China). *n*-Heptane (>99.0% purity) and all nitrates (>99.0% purity) were supplied by Shanghai Titan Scientific Co., Ltd. (Shanghai, China). 1-Hexene (>99.0% purity) was provided by Huawei Ruike Chemical Industry Co., Ltd. (Beijing, China). Three commercial zeolite X powder (without binder component) samples and four commercial binder-containing zeolite X products were used as references and the detailed information is given in Table S1. Deionized water was applied in all synthesis experiments. All chemicals were used without further purification.

2.2. Synthesis of Binderless Zeolite X Pellets. Binderless zeolite X pellets were prepared by modifying the method we reported earlier to synthesize zeolite A (see Figure 1).[35] First, a custom-made oil/water column for synthesis of the silica gel precursors was prepared. Specifically, the *water phase*: sodium aluminate alkaline solution (250 mL) was prepared by dissolving sodium metaaluminate (24.6 g) and sodium hydroxide (24 g) into deionized water (230 g). Saturated CTAB aqueous solution (15 mL) served as the *surfactant phase*, whereas *n*-heptane (30 mL) was employed as the *oil phase*. These three phases were successively added in a beaker. Subsequently, the silica gel mixture, which was obtained by stirring the mixture of silica sol (45 g) and ammonium chloride solution (10 g, 10 wt %), was dripped into the aforementioned custom-made column through a 0.35 mm (id) syringe needle in order to form spherical silica gel precursors of 2−3 mm in size. Subsequently, the alkaline solution at the bottom as well as the silica gel precursors obtained were separated from the oil/water column followed by transfer to a Teflon-lined stainless-steel autoclave. The molar composition of the prepared reaction system was $3Na_2O/Al_2O_3/2SiO_2/98H_2O$. After aging at 313 K for 0 to 6 h, the zeolite X products were crystallized at 373 K systematically for 0 to 24 h. Washing the samples was triplicated with deionized water. The resulting products were collected through filtration and dried at 373 K overnight.

2.3. Ion-Exchange of Synthesized Zeolite X Pellets. Various ions were introduced into the synthesized zeolite X pellets to obtain ion-exchanged zeolite X samples (see the detailed synthesis conditions in Table S2). Particularly, 25 g of BLZX pellets were immersed into 250 mL of $M(NO_3)_x$ ($M = Mg^{2+}$, Ca^{2+}, Co^{2+}, Ni^{2+}, Cu^{2+}, Zn^{2+} and Ag^+) aqueous solution (0.5 mol/L) under vigorous stirring at 333 K for 6 h. The ion-exchanged samples were washed with deionized water three times, separated by filtration, and dried in a vacuum oven at 373 K overnight.

2.4. Characterizations. Powder X-ray diffraction (XRD) patterns of all samples were obtained by employing a Bruker D8 ADVANCE X-ray diffractometer (Bruker AXS Inc., Germany) with Ni-filtered Cu Kα radiation (λ = 1.5418 Å) operated at 40 kV and 40 mA. The 2θ scanning angle recorded ranges from 5 to 60° with a step size of 0.02 and a rate of 5° per minute. All XRD patterns were analyzed using Jade 6.0 and the ICSD database for phase identification. Furthermore, the relative crystallinity was calculated by integrating the total characteristic diffraction peak areas of zeolite samples and using the commercial powder sample PZX-II as the reference.

The sample morphology was evaluated using a Nova NanoSEM 450 scanning electron microscope (SEM; FEI, USA) with an accelerating voltage of 15 kV and a beam current of 10 nA. Elemental analysis was carried out on a Falcon energy-dispersive spectrometer (EDS) (EDAX Inc., USA). Sputter-coating with a thin layer of platinum was adopted to avoid charging. Six measurement points were selected at different positions to obtain the average elemental composition for each sample.

High-resolution transmission electron microscopy (HRTEM) analyses were carried out on a JEM-2100 electron

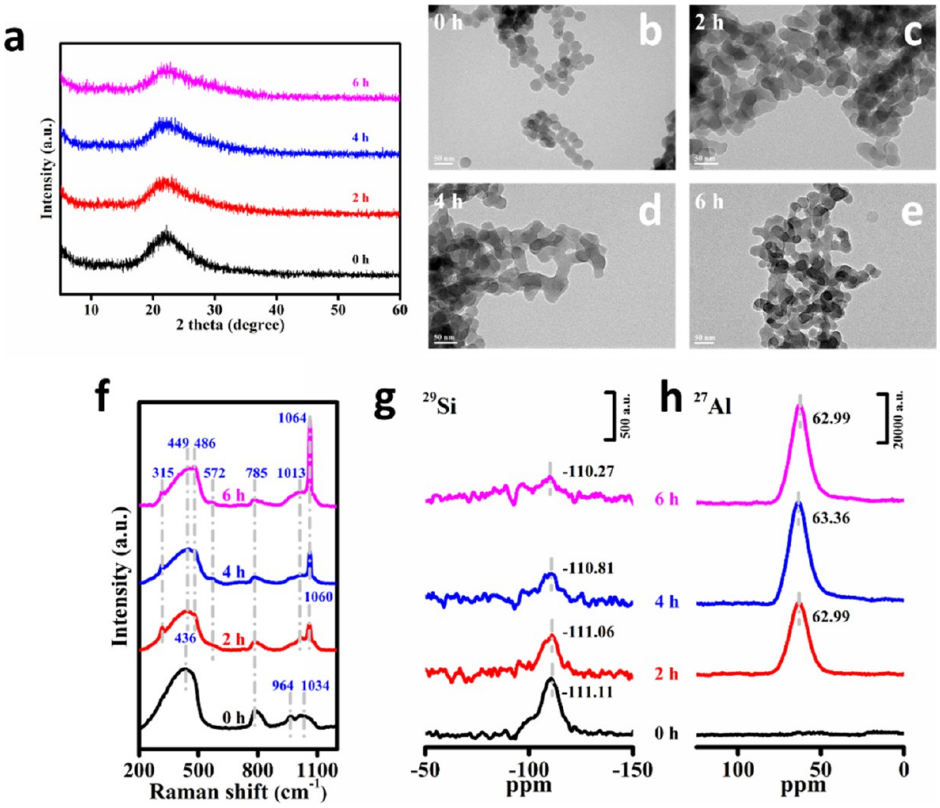

Figure 2. (a) XRD patterns, (b−e) TEM images, (f) UV-Raman and (g,h) NMR spectra of the amorphous aluminosilicate precursors with different aging lengths.

microscope (JEOL Co., Ltd., Tokyo, Japan) with an accelerating voltage of 200 kV. All samples were dispersed in absolute ethanol by ultrasonic treatment. Subsequently, the particle-suspended solution was dropped onto copper TEM grids coated with a holey carbon film and dried at room temperature.

The pore structure of each sample was measured by N_2 adsorption at 77 K using a 3H-2000PM2 automatic surface analyzer (BeiShiDe Instrument Co., Ltd., Beijing, China). The specific surface areas, micropore and mesopore volumes were calculated using the Brunauer−Emmett−Teller (BET), Horvath−Kawazoe (H−K) and Barrett−Joyner−Halenda (BJH) methods, respectively. Vapor adsorption of 1-hexene on zeolite X samples was determined under $P/P_0 = 0.85$ at 298 K using a 3H-2000PW gravimetric vapor adsorption analyzer (BeiShiDe Instrument Co., Ltd., Beijing, China). All samples were outgassed at 573 K for 12 h prior to adsorption measurements.

Raman spectra were collected by using a Renishaw InVia Reflex Lase Micro-Raman Spectrometer (Renishaw Plc., U.K.) equipped with a 325 nm argon ion laser. Data were recorded from 1200 to 200 cm^{-1} with a spectral resolution of 1.6 cm^{-1} and using a grating of 2400 lines·mm^{-1}.

Solid-state ^{29}Si and ^{27}Al magic angle spinning nuclear magnetic resonance (MAS NMR) spectra were recorded on a Bruker AVANCE-III 500 MHz super conducting Fourier NMR spectrometer (Bruker AXS Inc., Germany) with a 4 mm MAS probe. The CP method was used for the ^{29}Si MAS NMR analyses. The chemical shifts of ^{29}Si and ^{27}Al MAS NMR were externally referenced to tetramethylsilane (0 ppm) and 1 M $AlCl_3$ aqueous solution (0 ppm), respectively.

The maximum loads at crushing of zeolite X pellets were tested using a KQ-3 strength tester (Kehuan Analysis Technology Co., Ltd., Nanjing, China). The mechanical strengths of zeolite X pellets were evaluated by eq 1.

$$\sigma_m = 0.4P_m/\pi r^2 \qquad (1)$$

where P_m is the maximum load at crushing (N) and r is the radius of the zeolite X pellets (m).[36,37]

2.5. GCMC Simulation.

All computation simulations were performed using a sorption module in Materials Studio 7.0 package (Accelrys Inc., USA). The adsorption of 1-hexene on different ion-exchanged zeolite X structures was calculated based on the GCMC and configurational bias methods with periodic boundary conditions.[38]

The parent FAU framework topology was obtained from the Materials Studio database. According to the compositions of synthesized samples determined by EDS analyses (see Table S3), the Al atoms were randomly replaced by Si atoms, automatically following Lowenstein's Al−O−Al avoidance rule.[39] In addition, the corresponding extra-framework ion distribution was conducted by using the locate task in sorption module,[40,41] which can avoid the choice of ion amount at a specific position caused by the exchange of ion species.[42] The structural models of ion-exchanged zeolite X samples were enabled by replacing n Na^+ cations with n/x M^{x+} ones in a unit cell based on the found compositions. Moreover, the extra-framework ions incorporated in the zeolite structures can be Na^+, M^{x+}, or mixed cations. The Cartesian and fractional atomic positions were fixed during the simulation to restrict the adsorption in a specific region.

The 1-hexene module was built by a united-atom description, in which each CH_3 (sp^3), CH_2 (sp^3), CH (sp^2), and CH_2 (sp^2) group was treated as a single interaction center with effective potential parameters.[43] Table S4 lists the Lennard-Jones 12−6 potential parameters for 1-hexene groups and the charges for zeolite X framework system we used.[43,44] The Lennard-Jones potential parameters for zeolite X was obtained using the COMPASS force field,[45] which has a wide application in prediction of the covalent molecules' adsorption on FAU zeolite.[46,47] During simulation, all bond lengths were considered to be rigid, whereas bond angles were allowed to bend. Interactions among different sites were computed based on the standard Lorentz−Berthelot combining rule, and all interactions were cut off at a radius of 12.5 Å and a cubic spline truncation of 1 Å width. The Ewald summation method was used to handle the electrostatic interactions between guest and host atoms with an accuracy of 0.0001 kcal/mol. The guest−host potential energy and the density field of the guest molecules were sampled with 25 points between two evaluations of the field data on a three-dimensional grid of 0.25 Å spacing.

GCMC simulation was employed to calculate the adsorption capacity and interaction energy. The temperature (T), volume (V), and chemical potential (μ) of the system were fixed, whereas the system energy (E), pressure (P), and total number of molecules (N) varied. For each adsorption calculation point, the computational process was equilibrated during 5,000,000 steps and followed by 5,000,000 production steps for data collection. In order to validate the experimental results, the predicated simulation data were converted from absolute values to excess adsorption properties.

3. RESULTS AND DISCUSSION

3.1. Aging of Amorphous Aluminosilicate Precursors.

To understand the aging process of silica gel precursors in sodium aluminate alkaline solution, the as-synthesized samples with different aging times were characterized using integrated structural, microscopic, and spectroscopic methods. According to the XRD patterns in Figure 2a, the initially prepared silica gel precursors at the aging time of 0 h appear to be completely amorphous, which suggests the existence of initial silica nanoparticles in the precursors. The TEM images (see Figure 2b−e) further confirm the presence of spherical silica nanoparticles (~20 nm) in the as-prepared precursors. The Raman bands at 436, 785, 964, and 1034 cm^{-1} corresponding to the initial silica nanoparticles are observed in the Raman spectrum for the sample prior to aging (see Figure 2f). The broad band centered at 436 cm^{-1} is assigned to the bending mode of the Si−O−Si bond.[48] The band at 785 cm^{-1} can be attributed to the symmetric stretching mode of the Si−O−Si bond,[48] whereas the bands at 964 and 1034 cm^{-1} are associated with the asymmetric stretching mode of the Si−O−Si bond.[49] Additionally, the ^{29}Si MAS NMR spectrum in Figure 2g features a wide chemical shift at about −111.11 ppm, corresponding to the silica nanoparticles in the original silica gel precursors.[35] The absence of a ^{27}Al MAS NMR signal confirms a pure silica phase (see Figure 2h). Extended aging length leads to a slight decrease in XRD peak intensity for amorphous silica, which is further supported by the TEM images, clearly demonstrating the morphological transformations of silica nanoparticles in the sodium aluminate alkaline solution during the aging process. Specifically, as the aging length increases the dispersed silica nanoparticles gradually become coral-like amorphous aggregates without further crystallization. Such a phenomenon is consistent with the XRD results showing no evidence of long-range order.

As the aging time reaches 2 h, several weak Raman bands are detected in the region of 300 to 600 cm^{-1}, which correspond to different ring sizes.[50,51] The bands at 315 and 486 cm^{-1} can be ascribed to the bending modes of the T−O−T bond of the 6R and 4R, respectively, which indicates the formation of secondary building units (SBUs).[52] The 4R suggested by the Raman band at 486 cm^{-1} is probably dissociative, which is distinctly different from the rings in the zeolite X structure at around 500 cm^{-1}. The band at 572 cm^{-1} is associated with the Al−O−Si stretches of the aluminosilicate anions formed in alkaline solution.[53] Moreover, the bands at 436, 964, and 1034 cm^{-1} (for the original precursor sample) shift to 449, 1013, and 1060 cm^{-1} (for the sample at 2 h of aging time), respectively. Extended aging length leads to stronger Raman absorption at 486 and 1060 cm^{-1}, indicating gradual formation of 4R and T−O−T bonds during the aging process, respectively.

In the ^{29}Si MAS NMR spectra, the chemical shift at around −111 ppm gradually vanishes during the aging process because of the conversion of silica nanoparticles to aluminosilicate species. The ^{27}Al MAS NMR spectra show a chemical shift centered at ~63 ppm suggesting multiple chemical circumstances of Al species with the Al atom binding to different number of −O−Si− groups. As the aging time increases, the intensity of the peak at ~63 ppm increases, indicating continuous gelation of −O−Si− groups of silica precursors binding to Al species within the sodium aluminate alkaline solution. Such a reaction is primarily dominated by the diffusion of Al species into the silica gel precursor pellets. Interestingly, for all samples collected during aging, there is no characteristic Raman band corresponding to the D6R of zeolite X framework. We conclude that there is probably no crystalline phase formed during the aging process, and all samples appear to be completely amorphous, evidenced by the XRD and TEM results.

3.2. Crystallization of Zeolite X.

After aging, hydrothermal treatment was applied on the same reaction system (reactor) with amorphous aluminosilicate precursors to crystallize zeolite X at an elevated temperature. To reveal the compositional and structural evolutions the precursors undergo during *in situ* conversion to zeolite X, samples with different crystallization times (t_c) were collected and thoroughly characterized with structural, spectroscopic, and microscopic methods. Specifically, when t_c = 4 h, preliminary phase transition from the amorphous aluminosilicate aggregates to zeolite X crystals was observed (20.5% relative crystallinity) according to the XRD data shown in Figure 3. The morphological changes of crystallization initiated from the gel precursors are revealed by SEM and TEM images presented in Figures 4 and 5, respectively. It appears that the silica nanoparticles become denser aggregates, and partially crystallized particles from these aggregates were observed at t_c = 4 h.

The Raman bands at 290, 366, 504, 1000, and 1063 cm^{-1} (see Figure 6a) belonging to the framework structure of zeolite X are detected at t_c = 4 h.[54] Specifically, the sharp band at 504 cm^{-1} is assigned to the bending mode of the T−O−T bond of the 4R in the zeolite X structure.[52] The double bands at 290 and 366 cm^{-1} can be attributed to the bending modes of the T−O−T bond of D6R, which indicates initial crystallization of zeolite X. In contrast, the absence of these signals for the

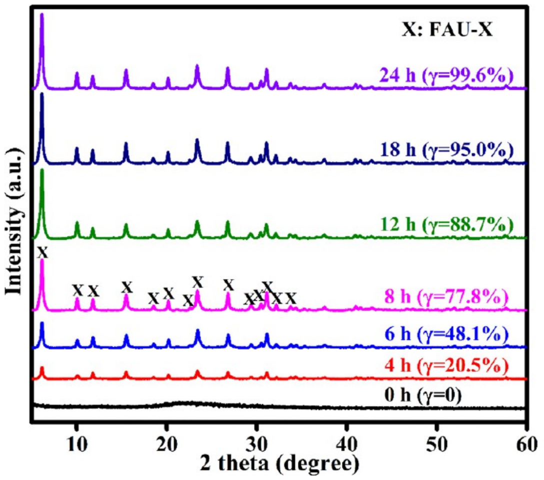

Figure 3. XRD patterns of the synthesized samples with different crystallization times.

sample at $t_c = 0$ h strongly suggests no zeolite X formation. Additionally, the bands at 1000 and 1063 cm^{-1} are ascribed to the asymmetric stretching vibration modes of the T−O−T bonds in the zeolite X framework.[52] Moreover, the Raman results also suggested formation of second structure units of 4R, 6R, and D6R when $t_c = 4$ h, implying the existence of an ordered crystalline zeolite X framework.

The ^{29}Si MAS NMR spectrum of the sample with t_c of 4 h presents chemical shifts at $\delta = -86.82, -91.00, -96.02$, and -100.44 ppm (see Figure 6b), which correspond to the Si−(O−Al)$_4$−, Si−(O−Al)$_3$−, Si−(O−Al)$_2$−, and Si−(O−Al)− (Si linking to different number of Al atoms by oxygen bridges) species, respectively.[55] The ^{27}Al MAS NMR spectra shown in Figure 6c present a significantly enhanced chemical shift at ~61 ppm owing to the binding of Al intermediate species with different numbers of −O−Si− groups.[35]

On the other hand, the development of the zeolite X phase was monitored by XRD as a function of crystallization time. First, characteristic patterns of zeolite X were confirmed for all samples investigated.[56] As crystallization proceeds, the relative crystallinity of zeolite X gradually increases until reaching the maximum at 24 h. Specifically, the samples with crystallization times of 6, 8, and 18 h have relative crystallinity of 48.1, 77.8, and 95.0%, respectively. Eventually, the relative crystallinity of sample crystallized up to 24 h is 99.6%.

From the SEM and TEM images presented in Figures 4 and 5, at $t_c = 8$ h, a number of crystals, from 300 to 500 nm in size, are observed within the gel precursors. This suggests the formation of zeolite X crystals accompanied by consumption of silica nanoparticles. Additionally, the Raman signals of 4R and D6R become stronger as crystallization time increases, clearly suggesting formation of the zeolite X structure. Meanwhile, the chemical shift at about −96 ppm in the ^{29}Si MAS NMR spectra becomes stronger as t_c increases, suggesting increase of the Si−(O−Al)$_2$− species population in the zeolite X framework. Moreover, all peaks in the ^{29}Si and ^{27}Al MAS NMR spectra retain their positions, whereas their intensities increase because of the increase of structural Si and Al species in the zeolite X framework. According to these results, the formation of the zeolite X framework is enabled through the self-aligned assemblage of the 4R, 6R, and D6R, accompanied with consumption of Si species in the silica gel precursors and transportation of Al species to the silica gel pellets.

According to these results, we deduce the mechanism of *in situ* hydrothermal conversion of silica gel precursors to binderless zeolite X pellets (see Figure 6d). First, in the low-temperature aging period, the precursors containing silica nanoparticles are converted to amorphous aluminosilicate aggregates by reacting with the Al species to form the primary building units (PBUs) of [SiO_4] and [AlO_4], in which the Al species diffuse from the bulk solution to the silica gel precursors accompanied with simultaneous formation of second building units (4R and 6R). During the crystallization process, D6R are created by interconnection between 6R and 4R, whereas the β cages are developed *via* self-assemblage of the second building units. Finally, the zeolite X framework is constructed through the reorganization of β cages with D6R. In our study, all these transformations take place *in situ* from the initial prepared silica gel precursors.

3.3. Kinetic Analysis of Crystallization.

To further understand the crystallization kinetics, the relative crystallinity of the synthesized samples is examined as a function of t_c. The aging time was fixed to be 6 h. The crystallization kinetic curve is well described by using the Avrami−Erofe'ev (A−E) expression (see eq 2).[57,58]

$$\gamma = [1 - \exp(-(k(t_c - \theta))^n)] \times 100\% \quad (2)$$

where γ is the relative crystallinity. k is the apparent rate constant of crystallization. t_c and θ are the times of crystallization and induction, respectively. n is the A−E exponent, a parameter related to the mechanism for nucleation and crystal growth.

By correlating the crystallization kinetics (see Figure S1 for the crystallization kinetics curve) with the A−E model, parameters including apparent rate constant k, induction time θ, and A−E exponent n were extracted from the fitting results (see Table 1). For the BLZX sample, the induction time θ is determined to be 0.81 h. As a result, the TEM image at t_c = 4 h (see Figure 5) presents partially crystallized morphology, because the sample has already experienced the induction period.[53]

3.4. Performance Evaluation.

1-Hexene vapor adsorption was carried out to determine the adsorption capacity of the BLZX sample. Several commercial zeolite X powder samples and binder-containing products were also tested for comparison. The BLZX sample exhibits comparable 1-hexene adsorption capacity to the zeolite X powder samples (see Figure 7a). Specifically, the adsorption capacities are 178.2 mg/g for the BLZX sample (Si/Al molar ratio = 1.46), 165.8 mg/g for PZX-I (Si/Al molar ratio = 1.23), 184.3 mg/g for PZX-II (Si/Al molar ratio = 1.41), and 176.9 mg/g for PZX-III (Si/Al molar ratio = 1.38). Moreover, the as-synthesized BLZX sample has a 20−35% higher adsorption capacity as compared to the four commercial binder-containing products, SZX-I−IV (having the adsorption values ranging from 117.9 to 141.2 mg/g) (see Figure 7b). Compared with the final product synthesized at t_c = 24 h (see Figure 4), the SEM images shown in Figure 7c reveal that the zeolite crystals of all binder-containing samples are covered with a large amount of binder, which has a significantly negative impact on the adsorption performance, for both capability and rate. Additionally, according to the pore structure analysis results listed in Table S5, all binder-containing samples present smaller BET-specific surface areas and total pore volumes compared with binderless zeolite X synthesized here. This can be ascribed to the dilution effect as well as filling of space among zeolite

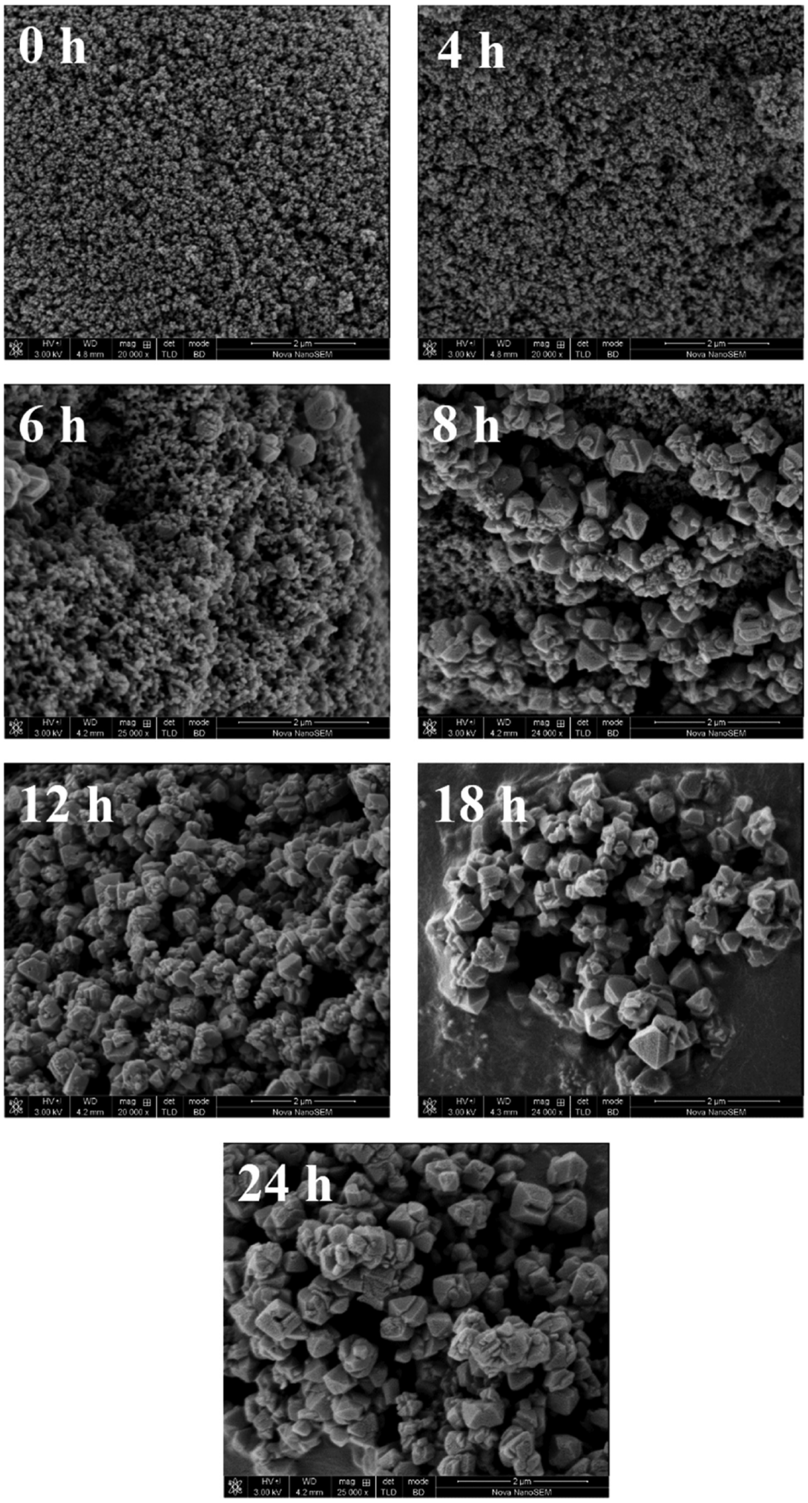

Figure 4. SEM images of the synthesized samples with different crystallization times.

crystals and added binder species.[35] Additionally, the mechanical strengths are observed to be 2.28 MPa for BLZX, 2.95 MPa for SZX-I, 2.79 MPa for SZX-II, 2.66 MPa for SZX-III, and 3.03 MPa for SZX-IV. Indeed, owing to the strong adhesion effect of the binder component, all commercial binder-containing zeolite samples show higher mechanical strength than that of the BLZX sample. However, the BLZX sample has a higher mechanical strength as compared with the binderless zeolite pellets synthesized *via* other methods. For example, the mechanical strengths of binderless microspheres of zeolite A and X are 1.79 and 0.46 MPa, respectively.[36,37] The mechanical strength of binderless zeolite 5A beads is 2.01 MPa.[59] Therefore, the binderless zeolite X we synthesized is a promising candidate for adsorption of olefin compounds with significantly enhanced capacity and affinity.

3.5. Tuning 1-Hexene Adsorption on Zeolite X *via* Ion-Exchange. To fine-tune the 1-hexene adsorption performance, we further modified the BLZX pellets by

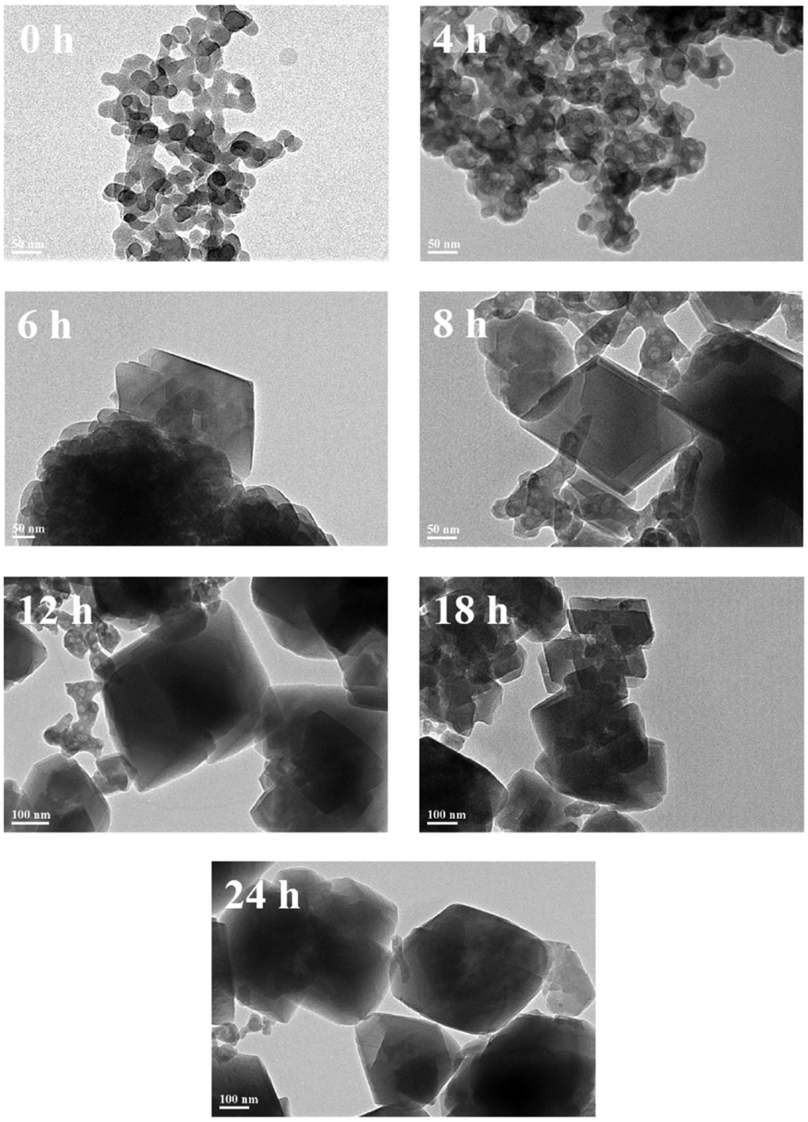

Figure 5. TEM images of the synthesized samples with different crystallization times.

postsynthesis ion-exchange with a series of metal nitrate solutions. The chemical compositions of all ion-exchanged zeolite X samples are listed in Table S3. The XRD patterns in Figure 8 confirm that all ion-exchanged binderless samples share characteristic FAU topology. However, decrease in peak intensity because of crystallinity loss can be observed for all ion-exchanged samples. Similar findings have been reported previously.[60] Among these ion-exchanged samples, Mg-BLZX and Ca-BLZX present a comparable XRD peak intensity as the parent BLZX sample with relative crystallinity of 89.4% (Mg-BLZX) and 81.3% (Ca-BLZX), whereas Co-BLZX, Cu-BLZX, Zn-BLZX, and Ag-BLZX exhibit crystallinity degradation of about 40%, with a relative crystallinity of 62.4% (Co-BLZX), 57.6% (Cu-BLZX), 61.5% (Zn-BLZX), and 60.3% (Ag-BLZX).

Introduction of Co^{2+}, Ni^{2+}, Cu^{2+}, Zn^{2+}, and Ag^{+} into the parent zeolite X decreases the BET-specific surface area and overall pore volume (see Table S5). This is primarily caused by the degradation in crystallinity during ion-exchange, suggested by the XRD results. In contrast, incorporation of divalent Mg^{2+} and Ca^{2+} into the zeolite X structure generates more free space when keeping the overall framework charge balanced, leading to increased BET-specific surface area and pore volume.[61] In addition, Mg-BLZX and Ca-BLZX show comparable crystallinity to that of the parent BLZX, and decrease in molecular weight (see Table S3 for chemical compositions of different samples) also accounts for the change in pore structure analysis results on a weight basis.

Vapor adsorption of 1-hexene was carried out to evaluate the adsorption capacity of ion-exchanged zeolite X samples (see Figure 9a for the experiment results). Compared with the as-synthesized BLZX (178.2 mg/g), six ion-exchanged samples have larger adsorption capacities. Specifically, they are 193.9 mg/g for Mg-BLZX, 181.7 mg/g for Ca-BLZX, 194.5 mg/g for Co-BLZX, 196.2 mg/g for Ni-BLZX, 185.2 mg/g for Cu-BLZX, and 182.0 mg/g for Zn-BLZX. The enhanced adsorption capacities of Mg-BLZX and Ca-BLZX samples are ascribed to the decrease in molecular weight as well as the increased pore volume ($0.313\ cm^3 \cdot g^{-1}$ for BLZX, $0.326\ cm^3 \cdot g^{-1}$ for Mg-BLZX, and $0.317\ cm^3 \cdot g^{-1}$ for Ca-BLZX). Unlike Mg-BLZX and Ca-BLZX samples, the enhanced adsorption capacities of Co, Ni, Cu, and Zn-exchanged samples are ascribed to the increase of adsorption centers (π-complexation) and interaction energy.[30] For Ag-BLZX, a 23.4% increase in molecular weight leads to significant decrease of

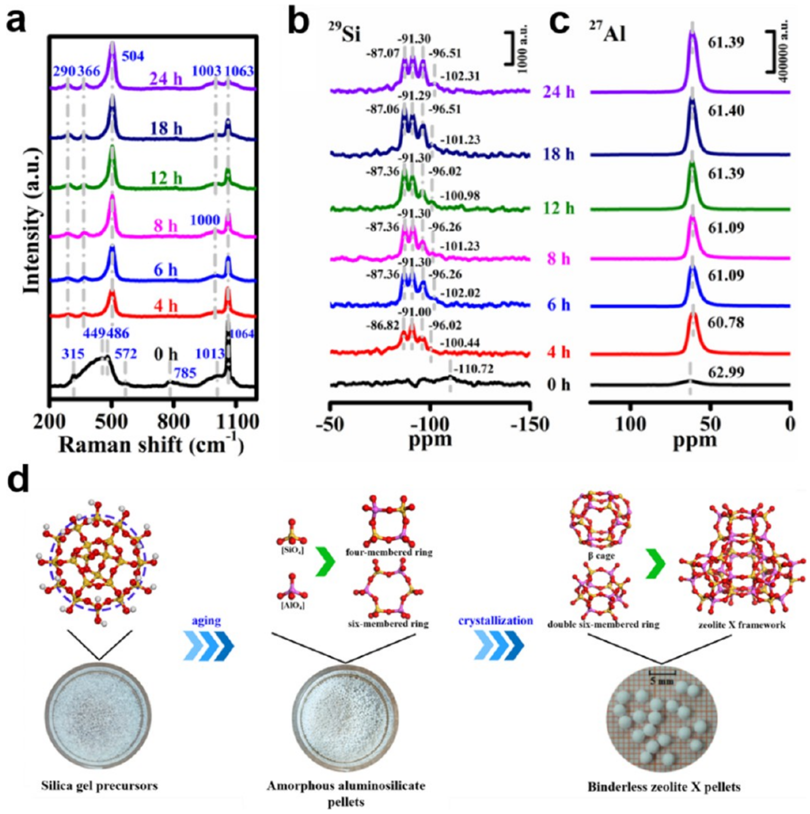

Figure 6. (a) UV-Raman and (b,c) NMR spectra of the hydrothermally synthesized samples with different crystallization times. (d) Mechanism deduced for *in situ* synthesis of binderless zeolite X pellets from silica gel precursors.

Table 1. A−E Model Parameters for *In Situ* Synthesis of Zeolite X

parameter	k (h^{-1})	θ (h)	n	R^2
value	0.16	0.81	1.93	0.99

1-hexene adsorption capacity. Furthermore, we used GCMC simulation to calculate the adsorption of 1-hexene on these ion-exchanged zeolite X samples. The unit cell structures are presented in Figure S2. Overall, the simulation results are consistent with the experimental data for all ion-exchanged samples (see Figure 9a).

To further evaluate the effect of ion-exchange on adsorption performance, the interaction energy between 1-hexene and zeolite was calculated by the locate task in the sorption module of the Accelrys Package (see Figure 9b). The adsorption process was strictly restricted to feature one 1-hexene molecule

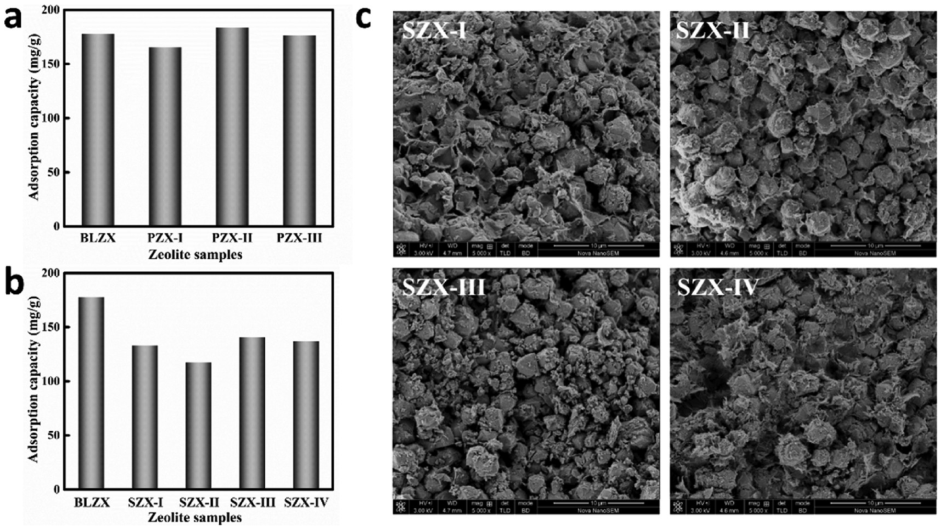

Figure 7. (a) 1-Hexene adsorption capacities on binderless zeolite X pellets and commercial zeolite X powder samples. (b) 1-Hexene adsorption capacities on binderless zeolite X pellets and commercial binder-containing zeolite X samples. (c) SEM images of commercial binder-containing samples.

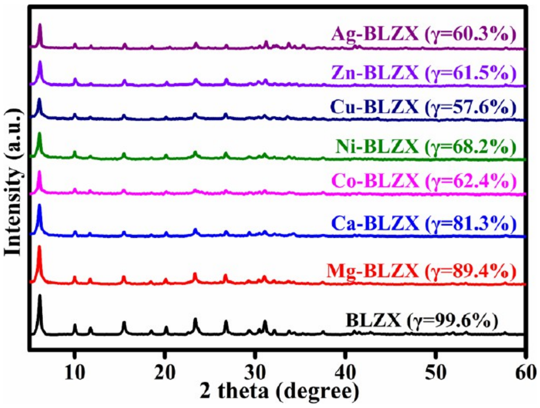

Figure 8. XRD patterns of different ion-exchanged zeolite X samples.

confined in each zeolite X cage to exclude the intermolecular force among adsorbates. According to the GCMC simulation results, introduction of Mg^{2+} and Ca^{2+} into zeolite X frameworks leads to decreased interaction energies from 52.22 kJ/mol for BLZX to 51.42 kJ/mol for Mg-BLZX and 50.97 kJ/mol for Ca-BLZX. Such a phenomenon is due to decrease in the number of adsorption sites.[62] In contrast, ion-exchange of Na^+ with Co^{2+}, Ni^{2+}, Cu^{2+}, Zn^{2+}, and Ag^+ increases the 1-hexene−zeolite X interaction energies to 54.10 kJ/mol for Co-BLZX, 56.20 kJ/mol for Ni-BLZX, 55.51 kJ/mol for Cu-BLZX, 53.09 kJ/mol for Zn-BLZX, and 56.66 kJ/mol for Ag-BLZX. Such enhancement is beneficial and will lead to more effective uptake of olefin from olefin/paraffin mixtures. Indeed, the enhanced guest−host interaction energies are due to π-complexation, which enables weak and reversible bonds between transition-metal ions and olefin molecules, resulting in olefin/paraffin separation with better selectivity.[63,64] According to the calculated interaction energies, compared with Co-BLZX, Cu-BLZX, and Zn-BLZX, the higher adsorption capacity seen on Ni-BLZX may be enabled by the interplays between more favorable cation-substituted structure and larger interaction energy.

The adsorption properties of zeolite X samples with different ion-exchange degrees were calculated to further evaluate the effects of ion type and degree of ion-exchange (see Figures 10 and 11). In summary, introduction of Mg^{2+} and Ca^{2+} into zeolite X leads to increased adsorption capacity because of pore volume increase, yet results in decrease in interaction energy. Indeed, such an effect tends to be more significant as the degree of Mg^{2+} and Ca^{2+} exchange increases. In contrast, for Co, Ni, Cu, and Zn-exchanged samples, as ion-exchange proceeds, the magnitudes of both 1-hexene adsorption capacity and interaction energy increase. This is mainly caused by the π-complexation among 1-hexene molecules and transition-metal ions. Moreover, the adsorption capacity of Ag-exchanged zeolite X decreases mainly because of the increase of molecular weight, whereas the magnitude of interaction energy increases owing to π-complexation. Generally, the impacts of ion-exchange degree on both adsorption capacity and interaction energy tend to be less significant as the ion-exchange reaches above 60%.

According to the calculated adsorption capacity, a fully Mg-exchanged sample presents the highest adsorption capacity of 195.0 mg/g. Interestingly, at a low ion-exchange degree of 12.8%, a Co-exchanged sample shows a higher uptake (178.5 mg/g) as compared to other partially cation-replaced samples at the same exchange level. Additionally, full replacement of Na^+ with Ag^+ in zeolite X leads to a decreased adsorption capacity of 115.1 mg/g. We also found that the calculated 1-hexene−zeolite X interaction energy at the same ion-exchanged degree follows the metal electronegativity order of Ag > Ni ≈ Co ≈ Cu > Zn > Mg > Ca. This is because in the zeolite X framework, a transition-metal ion with a greater electronegativity has a stronger bonding with 1-hexene.[64] We also noticed that metals with very high electronegativity values lead to poor (incomplete) regeneration.

In summary, according to our experimental and simulation results, Mg, Ca, Co, Ni, Cu, and Zn-exchanged samples exhibit higher adsorption capacities, and exchange of Co^{2+}, Ni^{2+}, Cu^{2+}, Zn^{2+}, and Ag^+ into zeolite X structure increases the interaction energy between 1-hexene and zeolite X. Ion-exchange enhances the adsorption performance of binderless zeolite X as a promising olefin/paraffin separation sorbent. On the other hand, our GCMC simulation provides experimental guidance to elucidate the relationships among ion type, exchange degree, and adsorption performance. This study has significant implications for the controllable preparation of function-strengthened porous materials for adsorption and may benefit chemical engineers by providing fundamental knowledge governing the performance of zeolite-based olefin/paraffin separation materials.

4. CONCLUSIONS

In this study, we demonstrate the feasibility of binderless zeolite X pellets' synthesis using the one-pot synthesis method. Precursors with different synthesis periods were fully

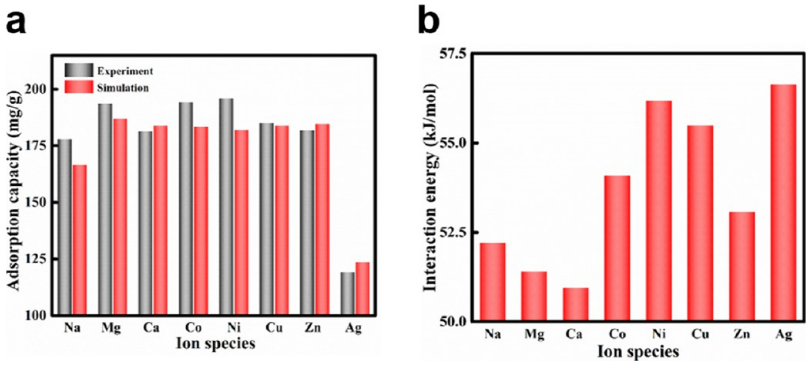

Figure 9. (a) Experimental and simulated 1-hexene adsorption capacity and (b) calculated 1-hexene−zeolite X interaction energies of various ion-exchanged zeolite X samples.

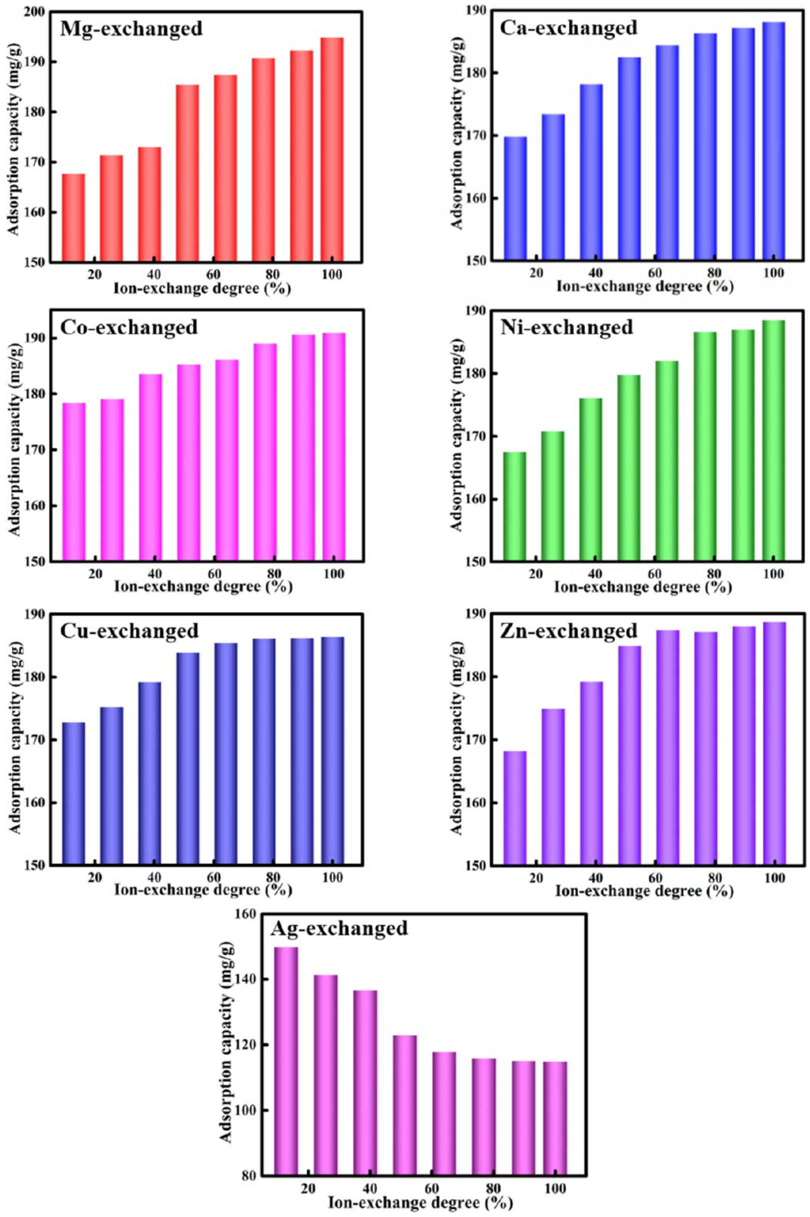

Figure 10. Calculated 1-hexene adsorption capacities *vs* degree of ion-exchange of zeolite X.

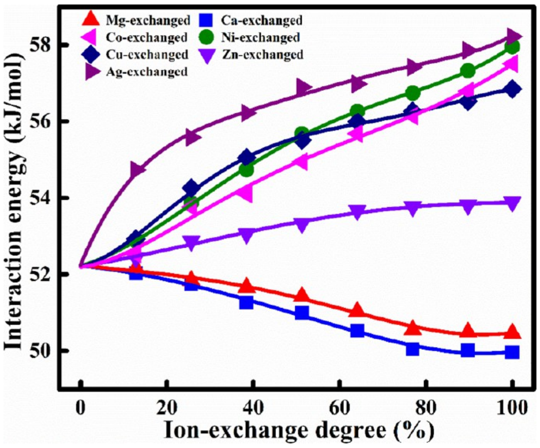

Figure 11. Calculated 1-hexene−zeolite interaction energies *vs* degree of ion-exchange of zeolite X.

characterized by multiple techniques to investigate both the aging and crystallization mechanisms, and to derive the crystallization kinetics. According to our results, the formation of 4R and 6R in aging are through effective linking among diffused Al species and dissolved Si species. Subsequently, zeolite X is crystallized through reorganization of β cages with D6R. In addition, we predict the adsorption capacity and interaction energy of 1-hexene adsorption using ion-exchanged zeolite X with different ion species and degrees of exchange *via* GCMC simulation. Mg and Ca-exchanged samples present a higher 1-hexene uptake, and Co, Ni, Cu, and Zn-exchanged samples show enhanced adsorption capacity and increased binding affinity with degree of ion-exchange. All these data strongly suggest that the postsynthesis ion-exchanged binderless zeolite X samples we reported here have a promising future to be applied as sorbents for olefin/paraffin separation.

■ ASSOCIATED CONTENT

Supporting Information

The Supporting Information is available free of charge at https://pubs.acs.org/doi/10.1021/acs.iecr.0c01049.

> Providers of different commercial zeolite X samples, detailed synthesis conditions, chemical compositions, Lennard-Jones potential parameters for 1-hexene groups, charges for zeolite X structures, pore structure analysis results, crystallization kinetics curve, and unit cell structures (PDF)

■ AUTHOR INFORMATION

Corresponding Authors

Hui Sun − *Petroleum Processing Research Center and International Joint Research Center of Green Energy Chemical Engineering, East China University of Science and Technology, Shanghai 200237, China;* orcid.org/0000-0002-8544-756X; Email: sunhui@ecust.edu.cn

Di Wu − *Alexandra Navrotsky Institute for Experimental Thermodynamics, The Gene and Linda Voiland School of Chemical Engineering and Bioengineering, Materials Science and Engineering, and Department of Chemistry, Washington State University, Pullman, Washington 99163, United States;* orcid.org/0000-0001-6879-321X; Email: d.wu@wsu.edu

Authors

Hao Jiang − *Petroleum Processing Research Center, East China University of Science and Technology, Shanghai 200237, China*

Dan Wang − *Petroleum Processing Research Center, East China University of Science and Technology, Shanghai 200237, China*

Jialun Tan − *Petroleum Processing Research Center, East China University of Science and Technology, Shanghai 200237, China*

Yuxiang Chen − *Petroleum Processing Research Center, East China University of Science and Technology, Shanghai 200237, China*

Yang An − *Petroleum Processing Research Center, East China University of Science and Technology, Shanghai 200237, China*

Yonghao Chen − *Petroleum Processing Research Center, East China University of Science and Technology, Shanghai 200237, China*

Yuan Wu − *Petroleum Processing Research Center, East China University of Science and Technology, Shanghai 200237, China*

Benxian Shen − *Petroleum Processing Research Center and International Joint Research Center of Green Energy Chemical Engineering, East China University of Science and Technology, Shanghai 200237, China*

Jichang Liu − *Petroleum Processing Research Center and International Joint Research Center of Green Energy Chemical Engineering, East China University of Science and Technology, Shanghai 200237, China;* orcid.org/0000-0002-5295-1778

Hao Ling − *Petroleum Processing Research Center and International Joint Research Center of Green Energy Chemical Engineering, East China University of Science and Technology, Shanghai 200237, China*

Jigang Zhao − *Petroleum Processing Research Center and International Joint Research Center of Green Energy Chemical Engineering, East China University of Science and Technology, Shanghai 200237, China;* orcid.org/0000-0002-2773-7200

Yujun Tong − *Sinopec Dalian Research Institute of Petroleum and Petrochemicals, Dalian Liaoning 116100, China*

Complete contact information is available at: https://pubs.acs.org/10.1021/acs.iecr.0c01049

Notes

The authors declare no competing financial interest.

■ ACKNOWLEDGMENTS

This work is financially supported by the National Natural Science Foundation of China (grant 21878097 and 91634112), SINOPEC (34400007-19-ZC0607-0117), and the Natural Science Foundation of Shanghai (grant 16ZR1408100). D.W. acknowledges the institutional funds from the Gene and Linda Voiland School of Chemical Engineering and Bioengineering, and the Alexandra Navrotsky Institute for Experimental Thermodynamics at Washington State University.

■ ABBREVIATIONS

4R	four-membered rings
6R	six-membered rings
D6R	double six-membered rings
MOFs	metal−organic frameworks
PZX-I−III	commercial zeolite X powder samples-I−III
SZX-I−IV	commercial spherical zeolite X samples-I−IV
BLZX	synthesized binderless zeolite X
XRD	powder X-ray diffraction
SEM	scanning electron microscope
EDS	energy-dispersive spectrometer
HRTEM	high-resolution transmission electron microscopy
BET	Brunauer−Emmett−Teller
H−K	Horvath−Kawazoe
BJH	Barrett−Joyner−Halenda
MAS NMR	magic angle spinning nuclear magnetic resonance
σ_m	mechanical strength
P_m	maximum load at crushing
r	radius of the zeolite X pellet
GCMC	grand canonical Monte Carlo
t_c	crystallization time
γ	relative crystallinity
PBUs	primary building units
SBUs	secondary building units
A−E	Avrami−Erofe'ev

■ REFERENCES

(1) Lin, R.-B.; Li, L.; Zhou, H.-L.; Wu, H.; He, C.; Li, S.; Krishna, R.; Li, J.; Zhou, W.; Chen, B. Molecular sieving of ethylene from ethane using a rigid metal-organic framework. *Nat. Mater.* **2018**, *17*, 1128−1133.

(2) Bae, Y.-S.; Lee, C. Y.; Kim, K. C.; Farha, O. K.; Nickias, P.; Hupp, J. T.; Nguyen, S. T.; Snurr, R. Q. High propene/propane selectivity in isostructural metal-organic frameworks with high densities of open metal sites. *Angew. Chem., Int. Ed.* **2012**, *51*, 1857−1860.

(3) Li, K.; Olson, D. H.; Seidel, J.; Emge, T. J.; Gong, H.; Zeng, H.; Li, J. Zeolitic imidazolate frameworks for kinetic separation of propane and propene. *J. Am. Chem. Soc.* **2009**, *131*, 10368−10369.

(4) Hou, J.; Liu, P.; Jiang, M.; Yu, L.; Li, L.; Tang, Z. Olefin/paraffin separation through membranes: from mechanisms to critical materials. *J. Mater. Chem. A* **2019**, *7*, 23489−23511.

(5) Corma, A.; Melo, F. V.; Sauvanaud, L.; Ortega, F. Light cracked naphtha processing: Controlling chemistry for maximum propylene production. *Catal. Today* **2005**, *107−108*, 699−706.

(6) Ren, T.; Patel, M.; Blok, K. Olefins from conventional and heavy feedstocks: Energy use in steam cracking and alternative processes. *Energy* **2006**, *31*, 425−451.

(7) Sholl, D. S.; Lively, R. P. Seven chemical separations to change the world. *Nature* **2016**, *532*, 435−437.

(8) Martins, V. F. D.; Ribeiro, A. M.; Kortunov, P.; Ferreira, A.; Rodrigues, A. E. High purity ethane/ethylene separation by gas phase simulated moving bed using ZIF-8 adsorbent. *AIChE J.* **2019**, *65*, No. e16619.

(9) Chu, S.; Cui, Y.; Liu, N. The path towards sustainable energy. *Nat. Mater.* **2017**, *16*, 16−22.

(10) Li, R.; Xing, H.; Yang, Q.; Zhao, X.; Su, B.; Bao, Z.; Yang, Y.; Ren, Q. Selective extraction of 1-hexene against *n*-hexane in ionic liquids with or without silver salt. *Ind. Eng. Chem. Res.* **2012**, *51*, 8588−8597.

(11) Bachman, J. E.; Kapelewski, M. T.; Reed, D. A.; Gonzalez, M. I.; Long, J. R. M_2 (m-dobdc) (M= Mn, Fe, Co, Ni) metal-organic frameworks as highly selective, high-capacity adsorbents for olefin/paraffin separations. *J. Am. Chem. Soc.* **2017**, *139*, 15363−15370.

(12) Martins, V. F. D.; Ribeiro, A. M.; Santos, J. C.; Loureiro, J. M.; Gleichmann, K.; Ferreira, A.; Rodrigues, A. E. Development of gas-phase SMB technology for light olefin/paraffin separations. *AIChE J.* **2016**, *62*, 2490−2500.

(13) Chen, Y.; Qiao, Z.; Lv, D.; Duan, C.; Sun, X.; Wu, H.; Shi, R.; Xia, Q.; Li, Z. Efficient adsorptive separation of C_3H_6 over C_3H_8 on flexible and thermoresponsive CPL-1. *Chem. Eng. J.* **2017**, *328*, 360−367.

(14) Kwon, H. T.; Jeong, H.-K. In situ synthesis of thin zeolitic-imidazolate framework ZIF-8 membranes exhibiting exceptionally high propylene/propane separation. *J. Am. Chem. Soc.* **2013**, *135*, 10763−10768.

(15) Bux, H.; Chmelik, C.; Krishna, R.; Caro, J. Ethene/ethane separation by the MOF membrane ZIF-8: molecular correlation of permeation, adsorption, diffusion. *J. Membr. Sci.* **2011**, *369*, 284−289.

(16) Hong, G. H.; Ji, D.; Kang, S. W. Highly permeable ionic liquid/Cu composite membrane for olefin/paraffin separation. *Chem. Eng. J.* **2013**, *230*, 111−114.

(17) Eldridge, R. B. Olefin/paraffin separation technology: a review. *Ind. Eng. Chem. Res.* **1993**, *32*, 2208−2212.

(18) Padin, J.; Rege, S. U.; Yang, R. T.; Cheng, L. S. Molecular sieve sorbents for kinetic separation of propane/propylene. *Chem. Eng. Sci.* **2000**, *55*, 4525−4535.

(19) Narin, G.; Martins, V. F. D.; Campo, M.; Ribeiro, A. M.; Ferreira, A.; Santos, J. C.; Schumann, K.; Rodrigues, A. E. Light olefins/paraffins separation with 13X zeolite binderless beads. *Sep. Purif. Technol.* **2014**, *133*, 452−475.

(20) Liu, J.; Calverley, E. M.; McAdon, M. H.; Goss, J. M.; Liu, Y.; Andrews, K. C.; Wolford, T. D.; Beyer, D. E.; Han, C. S.; Anaya, D. A.; Golombeski, R. P.; Broomall, C. F.; Sprague, S.; Clements, H.; Mabe, K. F. New carbon molecular sieves for propylene/propane separation with high working capacity and separation factor. *Carbon* **2017**, *123*, 273−282.

(21) Ma, X.; Lin, B. K.; Wei, X.; Kniep, J.; Lin, Y. S. Gamma-alumina supported carbon molecular sieve membrane for propylene/propane separation. *Ind. Eng. Chem. Res.* **2013**, *52*, 4297−4305.

(22) Cui, W. G.; Hu, T. L.; Bu, X. H. Metal-Organic Framework Materials for the Separation and Purification of Light Hydrocarbons. *Adv. Mater.* **2019**, *32*, 1806445.

(23) Sun, H.; Ren, D.; Kong, R.; Wang, D.; Jiang, H.; Tan, J.; Wu, D.; Chen, S.; Shen, B. Tuning 1-hexene/*n*-hexane adsorption on MOF-74 via constructing Co-Mg bimetallic frameworks. *Microporous Mesoporous Mater.* **2019**, *284*, 151−160.

(24) Weckhuysen, B. M.; Yu, J. Recent advances in zeolite chemistry and catalysis. *Chem. Soc. Rev.* **2015**, *44*, 7022−7024.

(25) Brosillon, S.; Manero, M.-H.; Foussard, J.-N. Mass transfer in VOC adsorption on zeolite: experimental and theoretical breakthrough curves. *Environ. Sci. Technol.* **2001**, *35*, 3571−3575.

(26) Nouar, F.; Eckert, J.; Eubank, J. F.; Forster, P.; Eddaoudi, M. Zeolite-likeMetal−Organic Frameworks (ZMOFs) as Hydrogen Storage Platform: Lithium and Magnesium Ion-Exchange and H_2-(rho-ZMOF) Interaction Studies. *J. Am. Chem. Soc.* **2009**, *131*, 2864−2870.

(27) Tan, Y.-X.; He, Y.-P.; Zhang, J. Pore partition effect on gas sorption properties of an anionic metal-organic framework with exposed Cu^{2+} coordination sites. *Chem. Commun.* **2011**, *47*, 10647−10649.

(28) Sakai, M.; Sasaki, Y.; Tomono, T.; Seshimo, M.; Matsukata, M. Olefin Selective Ag-Exchanged X-Type Zeolite Membrane for Propylene/Propane and Ethylene/Ethane Separation. *ACS Appl. Mater. Inter.* **2019**, *11*, 4145−4151.

(29) Anson, A.; Wang, Y.; Lin, C. C. H.; Kuznicki, T. M.; Kuznicki, S. M. Adsorption of ethane and ethylene on modified ETS-10. *Chem. Eng. Sci.* **2008**, *63*, 4171−4175.

(30) Abreu, N. J.; Valdés, H.; Zaror, C. A.; Azzolina-Jury, F.; Meléndrez, M. F. Ethylene adsorption onto natural and transition metal modified Chilean zeolite: An operando DRIFTS approach. *Microporous Mesoporous Mater.* **2019**, *274*, 138−148.

(31) Silva, J. A. C.; Schumann, K.; Rodrigues, A. E. Sorption and kinetics of CO_2 and CH_4 in binderless beads of 13X zeolite. *Microporous Mesoporous Mater.* **2012**, *158*, 219−228.

(32) Fakin, T.; Ristić, A.; Mavrodinova, V.; Zabukovec Logar, N. Highly crystalline binder-free ZSM-5 granules preparation. *Microporous Mesoporous Mater.* **2015**, *213*, 108−117.

(33) Schumann, K.; Unger, B.; Brandt, A.; Scheffler, F. Investigation on the pore structure of binderless zeolite 13Xshapes. *Microporous Mesoporous Mater.* **2012**, *154*, 119−123.

(34) Mehlhorn, D.; Valiullin, R.; Kärger, J.; Schumann, K.; Brandt, A.; Unger, B. Transport enhancement in binderless zeolite X- and A-type molecular sieves revealed by PFG NMR diffusometry. *Microporous Mesoporous Mater.* **2014**, *188*, 126−132.

(35) Sun, H.; Sun, Z.; Shen, B.; Liu, J.; Li, G.; Wu, D.; Zhang, Y. One-pot synthesis of binderless zeolite A spheres via in situ hydrothermal conversion of silica gel precursors. *AIChE J.* **2018**, *64*, 4027−4038.

(36) Yu, L.; Gong, J.; Zeng, C.; Zhang, L. Synthesis of monodisperse zeolite A/chitosan hybrid microspheres and binderless zeolite A microspheres. *Ind. Eng. Chem. Res.* **2012**, *51*, 2299−2308.

(37) Yu, L.; Gong, J.; Zeng, C.; Zhang, L. Synthesis of binderless zeolite X microspheres and their CO_2 adsorption properties. *Sep. Purif. Technol.* **2013**, *118*, 188−195.

(38) Accelrys. *Materials Studio, Modeling Getting Started*; Accelrys Software Inc.: San Diego, CA, 2004.

(39) Sanz, J.; Serratosa, J. M. ^{29}Si and ^{27}Al High-resolution MAS-NMR spectra of phyllosilicates. *J. Am. Chem. Soc.* **1984**, *106*, 4790−4793.

(40) Park, H. J.; Suh, M. P. Enhanced isosteric heat, selectivity, and uptake capacity of CO_2 adsorption in a metal-organic framework by impregnated metal ions. *Chem. Sci.* **2013**, *4*, 685−690.

(41) Jale, S. R.; Bülow, M.; Fitch, F. R.; Perelman, N.; Shen, D. Monte Carlo simulation of sorption equilibria for nitrogen and oxygen on LiLSX zeolite. *J. Phys. Chem. B* **2000**, *104*, 5272−5280.

(42) Zhu, L.; Seff, K. Reinvestigation of the crystal structure of dehydrated sodium zeolite X. *J. Phys. Chem. B* **1999**, *103*, 9512−9518.

(43) Nath, S. K.; Banaszak, B. J.; de Pablo, J. J. A new united atom force field for α-olefins. *J. Chem. Phys.* **2001**, *114*, 3612−3616.

(44) Calero, S.; Dubbeldam, D.; Krishna, R.; Smit, B.; Vlugt, T. J. H.; Denayer, J. F. M.; Martens, J. A.; Maesen, T. L. M. Understanding the role of sodium during adsorption: A force field for alkanes in sodium-exchanged faujasites. *J. Am. Chem. Soc.* **2004**, *126*, 11377−11386.

(45) Sun, H. COMPASS: an ab initio force-field optimized for condensed-phase applications overview with details on alkane and benzene compounds. *J. Phys. Chem. B* **1998**, *102*, 7338−7364.

(46) Jirapongphan, S. S.; Warzywoda, J.; Budil, D. E.; Sacco, A. Simulation of benzene adsorption in zeolite HY using supercage-based docking. *Microporous Mesoporous Mater.* **2006**, *94*, 358−363.

(47) Dang, S.; Zhao, L.; Gao, J.; Xu, C. Loading dependence of the adsorption mechanism of thiophene in FAU zeolite. *Ind. Eng. Chem. Res.* **2016**, *55*, 11801−11808.

(48) Garaga, M. N.; Persson, M.; Yaghini, N.; Martinelli, A. Local coordination and dynamics of a protic ammonium based ionic liquid immobilized in nano-porous silica micro-particles probed by Raman and NMR spectroscopy. *Soft Matter* **2016**, *12*, 2583−2592.

(49) Dutta, P. K.; Twu, J. Influence of framework silicon/aluminum ratio on the Raman spectra of faujasitic zeolites. *J. Phys. Chem.* **1991**, *95*, 2498−2501.

(50) Sharma, S. K.; Mammone, J. F.; Nicol, M. F. Raman investigation of ring configurations in vitreous silica. *Nature* **1981**, *292*, 140−141.

(51) Dutta, P. K.; Shieh, D. C.; Puri, M. Raman spectroscopic study of the synthesis of zeolite Y. *J. Phys. Chem.* **1987**, *91*, 2332−2336.

(52) Xiong, G.; Yu, Y.; Feng, Z.-c.; Xin, Q.; Xiao, F.-S.; Li, C. UV Raman spectroscopic study on the synthesis mechanism of zeolite X. *Microporous Mesoporous Mater.* **2001**, *42*, 317−323.

(53) Fan, F.; Feng, Z.; Li, G.; Sun, K.; Ying, P.; Li, C. In situ UV Raman spectroscopic studies on the synthesis mechanism of zeolite X. *Chem.—Eur. J.* **2008**, *14*, 5125−5129.

(54) Yu, Y.; Xiong, G.; Li, C.; Xiao, F.-S. Characterization of aluminosilicate zeolites by UV Raman spectroscopy. *Microporous Mesoporous Mater.* **2001**, *46*, 23−34.

(55) Lippmaa, E.; Maegi, M.; Samoson, A.; Tarmak, M.; Engelhardt, G. Investigation of the structure of zeolites by solid-state high-resolution ^{29}Si NMR spectroscopy. *J. Am. Chem. Soc.* **1981**, *103*, 4992−4996.

(56) Ma, Y.; Yan, C.; Alshameri, A.; Qiu, X.; Zhou, C.; Li, D. Synthesis and characterization of 13X zeolite from low-grade natural kaolin. *Adv. Powder Technol.* **2014**, *25*, 495−499.

(57) Finney, E. E.; Shields, S. P.; Buhro, W. E.; Finke, R. G. Gold nanocluster agglomeration kinetic studies: evidence for parallel bimolecular plus autocatalytic agglomeration pathways as a mechanism-based alternative to an avrami-based analysis. *Chem. Mater.* **2012**, *24*, 1718−1725.

(58) Zhang, R.-H.; Li, X.-K.; Cao, G.-P.; Shi, Y.-H.; Liu, H.-L.; Yuan, W.-K.; Roberts, G. W. Improved kinetic model of crystallization for isotactic polypropylene induced by supercritical CO_2: introducing pressure and temperature dependence into the avrami equation. *Ind. Eng. Chem. Res.* **2011**, *50*, 10509−10515.

(59) Mendes, P. A. P.; Ribeiro, A. M.; Gleichmann, K.; Ferreira, A. F. P.; Rodrigues, A. E. Separation of CO_2/N_2 on binderless 5A zeolite. *J. CO_2 Util.* **2017**, *20*, 224−233.

(60) Chen, X.; Shen, B.-x.; Sun, H.; Zhan, G.-x.; Huo, Z.-z. Adsorption and its mechanism of CS_2 on ion-exchanged zeolites Y. *Ind. Eng. Chem. Res.* **2017**, *56*, 6499−6507.

(61) Chen, X.; Shen, B.; Sun, H.; Zhan, G. Ion-exchange modified zeolites X for selective adsorption desulfurization from Claus tail gas: Experimental and computational investigations. *Microporous Mesoporous Mater.* **2018**, *261*, 227−236.

(62) Zhang, J.; Burke, N.; Yang, Y. Molecular Simulation of Propane Adsorption in FAU Zeolites. *J. Phys. Chem. C* **2012**, *116*, 9666−9674.

(63) Dewar, M. J. S. A review of the π-complex theory. *Bull. Soc. Chim. Fr.* **1951**, *18*, C71−C79.

(64) Faiz, R.; Li, K. Olefin/paraffin separation using membrane based facilitated transport/chemical absorption techniques. *Chem. Eng. Sci.* **2012**, *73*, 261−284.